



Research
AI for Process Manufacturing—Article

A Multi-Scale Graph Neural Network for the Prediction of Multi-Component Gas Adsorption

Lujun Li^{a,b,c}, Haibin Yu^{b,c,*}

^a Department of Automation, University of Science and Technology of China, Hefei 230026, China

^b State Key Laboratory of Robotics, Shenyang Institute of Automation, Chinese Academy of Sciences, Shenyang 110016, China

^c Key Laboratory of Networked Control Systems, Chinese Academy of Sciences, Shenyang 110016, China



ARTICLE INFO

Article history:

Received 30 August 2024

Revised 2 May 2025

Accepted 15 August 2025

Available online 19 August 2025

Keywords:

Metal–organic frameworks

Multi-head attention score

Graph neural network

Adsorption

ABSTRACT

Metal–organic frameworks (MOFs) hold great potential for gas separation and storage, and graph neural networks have proven to be a powerful tool for exploring material structure–property relationships and discovering new materials. Unlike traditional molecular graphs, crystal graphs require consideration of periodic invariance and modes. In addition, MOF structures such as covalent bonds, functional groups, and global structures impact adsorption performance in different ways. However, redundant atomic interactions can disrupt training accuracy, potentially leading to overfitting. In this paper, we propose a multi-scale crystal graph for describing periodic crystal structures, modeling interatomic interactions at different scales while preserving periodicity invariance. We also propose a multi-head attention crystal graph network in multi-scale graphs (MHACGN-MS), which learns structural characteristics by focusing on interatomic interactions at different scales, thereby reducing interference from redundant interactions. Using MOF adsorption for gases as an example, we demonstrate that MHACGN-MS outperforms traditional graph neural networks in predicting multi-component gas adsorption. We also visualize attention scores to validate effective learning and demonstrate the model's interpretability.

© 2025 THE AUTHORS. Published by Elsevier LTD on behalf of Chinese Academy of Engineering and Higher Education Press Limited Company. This is an open access article under the CC BY-NC-ND license (<http://creativecommons.org/licenses/by-nc-nd/4.0/>).

1. Introduction

Metal–organic frameworks (MOFs) are unique porous crystalline materials with extensive applications in gas storage [1,2], separation [3,4], catalysis [5,6], and sensing [7,8]. They consist of metal nodes and organic connectors, which form diverse porous structures with varied physical and surface chemical properties. Experimental research on MOFs, particularly regarding their gas adsorption properties, is costly and time-consuming. Simulation methods such as molecular dynamics (MD) [9] and grand canonical Monte Carlo (GCMC) [10] are used to obtain gas adsorption properties, but their computational costs limit large-scale material screening.

The advent of extensive experimental and computational databases has ushered in a new era in materials science, with artificial intelligence (AI) methodologies revolutionizing the prediction of material properties. Techniques such as decision trees [11,12], ran-

dom forests [13,14], Gaussian process regression [15,16], support vector machines [17,18], multi-layer perceptrons (MLPs) [19,20], graph convolutional neural networks (GCNNs) [21,22], and transfer learning [23,24] leverage vast amounts of data to develop precise prediction models, enabling rapid and accurate predictions of gas adsorption properties in MOFs. These models increase research efficiency and support large-scale screening [25].

However, challenges persist in the characterization of crystalline materials and interpretation of structure–activity relationships. Traditional descriptors used with machine learning algorithms focus narrowly on single aspects of crystal properties, neglecting holistic spatial configurations and interatomic interactions. Moreover, strong correlations among structural descriptors limit prediction accuracy improvements through descriptor augmentation.

Graph neural networks have been introduced as a means of addressing these problems. However, crystals are periodic and infinitely repetitive, so traditional graph neural networks such as graph isomorphism networks (GINs) [26], graph convolutional networks (GCNs) [27], and graph attention networks (GATs) [28] are not suitable for the learning of crystal structures. Instead,

* Corresponding author.

E-mail address: yhb@sia.cn (H. Yu).

researchers have introduced crystallographic neural network algorithms. Algorithms such as crystal graph convolutional neural networks (CGCNNs) [29], materials graph network (MEGNet) [30], message-passing neural networks (MPNNs) [31], and MatFormer [32] capture both periodic and cell three-dimensional Euclidean group (E(3)) invariance. These graph neural networks offer reliable methods for predicting crystal performance. However, CGCNNs, MatFormer, and MEGNet primarily focus on inorganic crystals from the Materials Project and the Joint Automated Repository for Various Integrated Simulations (JARVIS) databases, while MPNNs target small organic molecules from the Quantum Machine 9 (QM9) database. MOFs are crystalline materials with complex periodic network structures formed by metal ions/clusters and organic ligands. As MOFs are more complex in structure than traditional inorganic crystalline materials, directly applying such methods to MOFs may yield unsatisfactory results, with a possible risk of overfitting.

The current graph neural network algorithms used for MOFs typically concatenate descriptors or molecular fingerprints as global features into the neural network, resulting in satisfactory performance [33,34]. Research indicates that accuracy can also be achieved using only these descriptors or fingerprints as input, without crystal image data. This finding raises questions about whether the success of such graph neural networks stems from these descriptors/fingerprints or from truly learning the spatial conformation and interatomic interactions of crystalline materials at different scales, which is the primary goal of crystal graph neural network applications.

This study introduces a multi-head attention crystal graph network in multi-scale graphs (MHACGN-MS), a crystal graph neural network model, to alleviate the existing limitations:

(1) We adopt a radius-based multi-scale graph construction method to ensure periodicity and cell E(3) invariance, encode periodic patterns, and decompose complex crystal graphs into simpler subgraphs based on atomic interactions at different scales.

(2) MHACGN-MS integrates a multi-head self-attention mechanism and graph pooling to learn atomic interactions and structural features, eliminate redundant interference, and simplify neural network structures, ensuring the targeted capture of covalent bonds, functional groups, global structures, and other features at different scales across various subgraphs.

(3) We validate our neural network by using it to predict the MOFs' adsorption of gases composed of different components, thereby demonstrating the generality and high accuracy of MHACGN-MS.

(4) We visualize the attention scores assigned to interatomic interactions at various scales and find that the attention scores assigned to interatomic interactions at adsorption sites are significantly higher, indicating that MHACGN-MS has indeed learned the spatial conformation and interatomic interactions of crystals.

2. Materials and calculation

2.1. Dataset construction

This research used the MOFs from the computation-ready, experimental (CoRE) MOF databases [35]. Compared with a hypothetical MOF database, all MOF structures in the CoRE MOF databases are derived from synthetic materials, and synthesis schemes are generally available. In addition, relevant calculation research has demonstrated the practicability of the CoRE MOF databases [36]. All the parameters we used were calculated via the Zeo++ [37] software package using a helium atom (with the kinetic diameter of 2.58 Å) as a probe.

2.2. Grand canonical Monte Carlo simulations

GCMC simulations [38] using RASPA 2.0 [39] were used to calculate the MOF adsorption capacities with the parameter settings outlined in Table 1, yielding gas adsorption capacities as dataset labels. Lennard–Jones (LJ) potential parameters for the MOFs were derived from the universal force field (UFF) [40]. The accuracy of the UFF was supported by agreement with the experimental adsorptions of CO₂, N₂, and CH₄ [41–43], making the UFF suitable for the high-throughput screening of MOFs. Gas parameters were described using Transferable Potentials for Phase Equilibria (TraPPE) [44], and LJ parameters between the MOFs and gases were calculated using the Lorentz–Berthelot rules. All force field parameters are provided in Section S1 in Appendix A. An adaptive cut-off radius based on MOF unit cell size was applied, with the simulation cell expanded and periodic boundary conditions enforced.

For the GCMC simulations of single-component gas adsorption, we employed 2000 initialization cycles, 5000 balancing cycles, and 5000 production cycles. For each MOF, we uniformly sampled 5 points within the 6–30 bar (1 bar = 10⁵ Pa) range, calculated the adsorption using GCMC, and plotted the adsorption. Similarly, for multi-component gas adsorption, we used the same cycle configuration and sampled 5 points within the 0.1:0.9 to 0.5:0.5 ratio range for each MOF, again calculating and plotting the adsorption. In the GCMC simulation system, electrostatic interactions between gas molecules and MOF materials were evaluated using the four molecular movement modes of translation, reinsertion, rotation, and exchange in each cycle. While some discrepancies were noted between the experimental and GCMC-calculated adsorption for MOFs, the trend accuracy of GCMC was reliable.

3. Construction of a multi-scale crystal graph

In this section, we delineate the concepts of unit cell E(3) invariance, periodic invariance, and the encoding of periodic patterns [32]. We also present a multi-scale crystal graph that embodies periodic invariance and encapsulates periodic patterns.

MOFs are composed of the smallest crystal cells that repeat themselves in a regular lattice configuration within 3D space. In this scenario, $(\mathbf{A}, \mathbf{P}, \mathbf{L})$ is given as the representative notation for MOFs. The atomic feature matrix is $\mathbf{A} = [\mathbf{a}_1, \mathbf{a}_2, \dots, \mathbf{a}_i, \dots, \mathbf{a}_M]^T \in \mathbb{R}^{M \times d_a}$, where M is the number of atoms in the cell, $\mathbf{a}_i \in \mathbb{R}^{d_a}$ is the feature vector of atom i , and d_a is the dimension of feature vector \mathbf{a}_i . $\mathbf{P} = [p_1, p_2, \dots, p_i, \dots, p_M]^T \in \mathbb{R}^{M \times 3}$ is the position matrix, where $p_i \in \mathbb{R}^3$ represents the cartesian coordinates for atom i . $\mathbf{L} = [\ell_1, \ell_2, \ell_3]^T \in \mathbb{R}^{3 \times 3}$ is the lattice matrix, used to describe how the crystal cell repeats itself in the three directions ℓ_1 , ℓ_2 , and ℓ_3 . The lattice basis vectors ℓ_1 , ℓ_2 , and ℓ_3 are three non coplanar vectors in three-dimensional space that form the edge vectors of the unit cell. Formally, the infinite crystal structure can be represented as follows:

Table 1

Evaluation criteria used to assess the effectiveness of MOFs for gas adsorption isotherms.

Gas composition	Temperature (K)	Pressure range (bar ^a)	Gas ratio range
Single-component gas adsorption			
CO ₂	298	6–30	–
CH ₄	298	6–30	–
N ₂	298	6–30	–
Multi-component gas adsorption			
CO ₂ :N ₂	298	–	0.1:0.9 to 0.5:0.5
CO ₂ :CH ₄	298	–	0.1:0.9 to 0.5:0.5
CH ₄ :N ₂	298	–	0.1:0.9 to 0.5:0.5

^a 1 bar = 10⁵ Pa.

$$\begin{aligned}\widehat{\mathbf{P}} &= \{\widehat{p}_i | \widehat{p}_i = p_i + k_1 \ell_1 + k_2 \ell_2 + k_3 \ell_3, k_1, k_2, k_3 \in \mathbb{Z}, 1 \leq i \leq M\} \\ \widehat{\mathbf{A}} &= \{\widehat{a}_i | \widehat{a}_i = \mathbf{a}_i, i \in \mathbb{Z}, 1 \leq i \leq M\}\end{aligned}\quad (1)$$

where $\widehat{\mathbf{P}}$ is an infinite set of all possible three-dimensional locations for each atom i within the expansive infinite crystal lattice, whereas $\widehat{\mathbf{A}}$ is an infinite set of the atomic features for each atom i within the infinite crystal lattice.

Given the inability to articulate the infinite crystal structure, the construction of a MOF's crystal graph must aptly represent the periodic structure of the MOF by adhering to the invariance of the crystal cell $E(3)$ and the periodicity invariance, and by encompassing sensible periodic patterns.

3.1. Introduction of unit cell $E(3)$ invariance

The function $f: (\mathbf{A}, \mathbf{P}, \mathbf{L}) \rightarrow X$ is unit cell $E(3)$ invariant such that, for all $\mathbf{Q} \in \mathbb{R}^{3 \times 3}$, $|\mathbf{Q}| = 1$, and $b \in \mathbb{R}^3$, $f(\mathbf{A}, \mathbf{P}, \mathbf{L}) = f(\mathbf{A}, \mathbf{QP} + b, \mathbf{QL})$, where \mathbf{Q} represents the rotation operation, and b represents the translation operation. X refers to the mapping space of function $f(\cdot)$, which is an abstract mathematical representation of the overall structure of the crystal graphs. For function $f(\cdot)$ satisfying unit cell $E(3)$ invariant, the mapping spaces X corresponding to $f(\mathbf{A}, \mathbf{P}, \mathbf{L})$ and $f(\mathbf{A}, \mathbf{QP} + b, \mathbf{QL})$ are identical.

Whether rotation and reflection are applied together to \mathbf{P} (the position matrix) and \mathbf{L} (the lattice matrix), or only translation is applied to \mathbf{P} , the structure of the elements should remain unchanged.

3.2. Introduction of periodic invariance

The function $f: (\mathbf{A}, \mathbf{P}, \mathbf{L}) \rightarrow X$ is periodic invariant if $f(\mathbf{A}, \mathbf{P}, \mathbf{L}) = f(\phi(\widehat{\mathbf{A}}, \widehat{\mathbf{P}}, \alpha \mathbf{L}, p_c), \alpha \mathbf{L})$ holds for all $p_c \in \mathbb{R}^3$ and $\alpha \in \mathbb{N}_+^3$. p_c is the position of corner point referring to the vertex of a unit cell. We define a function $\phi(\widehat{\mathbf{A}}, \widehat{\mathbf{P}}, \alpha \mathbf{L}, p_c) \rightarrow (\mathbf{A}, \mathbf{P})$ to simulate how to form different unit cells from a given infinite crystal structure. For an infinite crystal structure represented as $(\widehat{\mathbf{A}}, \widehat{\mathbf{P}})$, $\phi(\cdot)$ uses a corner point p_c and shape matrix $\alpha \mathbf{L}$ to form a unit cell represented as (\mathbf{A}, \mathbf{P}) . The notation $\alpha \in \mathbb{N}_+^3$ denotes ordered triplets composed of three positive integers, which signify the scaling up of a repeating unit cell generated by periodic boundaries. For the infinite crystal, altering the periodic boundary results in different unit cell structures. To circumvent this issue, the concept of peri-

odic invariance is introduced: When the periodic boundary is shifted or enlarged, the representation of periodic invariance should remain consistent.

The periodic pattern is defined by the size and direction of the lattice matrix $\mathbf{L} = [\ell_1, \ell_2, \ell_3]^T \in \mathbb{R}^{3 \times 3}$, demonstrating how the minimum repeatable structure (\mathbf{A}, \mathbf{P}) can self-expand in infinite 3D space. Different periodic patterns may indicate different materials.

3.3. Radius-based graph construction

For the graph construction of MOFs, we introduce a radius-based method, treating node i as atomic i and its duplicates to ensure period invariance (proven in Section S2 in Appendix A). Within the given radius in Fig. 1, we form the neighborhood of node i by selecting t -nearest neighbors based on geometric distance. However, this approach treats the crystal as a finite structure, capturing only interactions within the given radius and neglecting periodic patterns. To better represent the infinite crystal structure, periodic patterns should be explicitly considered in crystal learning.

In this paper, we employed the method proposed by Yan et al. [32] to encode the periodic patterns of crystal structures by adding self-connection edges. Encoding repetitive periodic patterns requires consideration of the relative positions between atoms and their nearby repeating atoms. For instance, given an atom i with position p_i and lattice matrix $\mathbf{L} = [\ell_1, \ell_2, \ell_3]^T \in \mathbb{R}^{3 \times 3}$, we considered its three duplicate atoms at positions $p_i + \ell_1$, $p_i + \ell_2$, and $p_i + \ell_3$ to encode the periodic pattern. To mitigate the high computational complexity associated with orientation information in the vectors ℓ_i , we employed six geometric distances, denoted as $\|\ell_1\|_2$, $\|\ell_2\|_2$, $\|\ell_3\|_2$, $\|\ell_1 + \ell_2\|_2$, $\|\ell_1 + \ell_3\|_2$, and $\|\ell_2 + \ell_3\|_2$, to determine the angles between any two vectors in \mathbf{L} . Specifically, the angle between ℓ_1 and ℓ_2 can be calculated using $\|\ell_1\|_2$, $\|\ell_2\|_2$, and $\|\ell_1 + \ell_2\|_2$. We constructed these six geometric distances as self-connecting edges for node i , effectively encoding the periodic pattern present in the lattice matrix \mathbf{L} into the crystal graph. An illustration of the constructed graph in a two-dimensional (2D) scenario is presented in Fig. 1.

3.4. Multi-scale crystal graph construction

MOFs exhibit intricate correlations between their structure and their functional characteristics. Taking adsorption performance as an example, key structural factors that influence physical adsorption include open metal sites, functional groups, pore structure, and other structural features at various scales. Our objective was

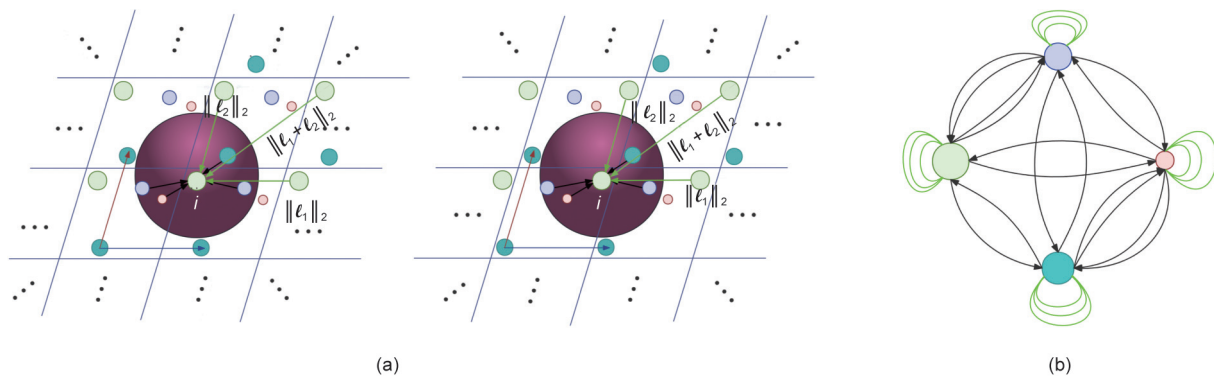


Fig. 1. Illustrations depicting the radius-based method employed for graph construction and the encoding of periodic patterns in graph construction for a two-dimensional (2D) scenario. Black arrows represent the edges formed through radius-based graph construction, while green arrows indicate self-connecting edges. (a) Illustration showing that the use of self-connected edges in radius-based graph construction for encoding periodic patterns ensures periodic invariance. $\|\cdot\|_2$ stands for geometric distance. (b) Illustration of the constructed graph incorporating periodic pattern encoding for the aforementioned 2D case.

to investigate crystal structure characteristics across different scales, minimize redundant information, accurately identify spatial atomic interactions, and ensure model interpretability.

To achieve this objective, we defined sensing distances for MOF atoms with geometric lengths corresponding to open metal site/bond detection, functional group/surface detection, and pore structure/topology detection, respectively.

Since the bond length of a coordination bond is usually around 2 Å, we set the range of the first level of attention's scale radius to (0, 2 Å] in order to focus on the feature learning of open metal sites within MOFs. Functional groups are atoms or atomic groups that determine the chemical properties of organic compounds. Based on the atomic composition of common functional groups in MOFs that affect adsorption (e.g., carboxyl, amino, nitro, and hydroxyl groups, nitrogen-containing heterocycles), we set the range of the second level of attention's scale radius to (2 Å, 3 Å] in order to focus on the feature learning of functional groups. Regarding the learning of specific surface area and pore structure, the pore diameters of microporous MOFs used for gas adsorption are generally less than 20 Å. Therefore, we set the upper limit of the scale radius range for the third level of attention to 5–10 Å. After multiple attempts and comparisons, we found that the prediction effect was best when the upper limit was set to 5 Å. We speculate that an attention range with a radius of 5 Å is sufficient to learn the features of the specific surface area and pore structure. Moreover, when the upper limit is set to 10 Å, the generated crystal subgraphs become more complex, resulting in more interference in feature learning and increased computational time. Therefore, we ultimately set the range of the third level of attention's scale radius to (3 Å, 5 Å].

Edges (excluding self-connected edges) meeting these perceptual distances in the crystal graph were classified, and three subgraphs were established accordingly. Each subgraph retained self-connected edges to ensure periodic patterns. A multi-scale subgraph constructed in 2D is shown in Fig. 2. Notably, multi-scale subgraphs maintain period invariance well, as the subgraphs are consistent for the same perceived distance.

Graph construction comprised three essential stages: periodic invariant graph construction, periodic pattern coding, and multi-scale subgraph construction. In the first stage, we proved that

graph construction based on radius satisfies period invariance, as outlined in Section S2. In the second stage, we encoded periodic patterns into the graph by introducing self-connected edges, ensuring that period invariance was not disrupted. The resulting 2D graph is presented in Fig. 1(b). In the third stage, we constructed multi-scale graphs to facilitate the targeted learning of critical structural features affecting adsorption performance at different scales, while preserving period invariance and retaining periodic patterns. The 2D subgraphs are shown in Fig. 2.

4. The proposed multi-head attention crystal graph network in multi-scale graphs

Drawing upon this crystal graph, we propose MHACGN-MS, a sophisticated multi-scale graph neural network architecture that integrates a self-attention mechanism within its graph pooling layers. In this representation, each $\mathbf{a}_i \in \mathbf{A}$ corresponds to the d_a -dimensional feature vector of atom i , as illustrated in Fig. 3. Additionally, $\mathbf{e}_{ij}^{h(r_1, r_2)} \in \mathbb{R}^{d_e}$ is the edge feature vector represents the d_e -dimensional feature vector of the h th edge connecting nodes i and j in range $(r_1, r_2]$, $(r_1, r_2] = (0, 2], (2, 3]$, and $(3, 5]$. d_e is the dimension of edge feature vector. The information transmission of our algorithm framework consists of three steps: ① edge attention score calculation, ② edge selection, and ③ node update.

4.1. Edge attention score calculation

The multi-head attention mechanism has demonstrated effectiveness in various deep-learning frameworks, enabling the network to prioritize essential features while minimizing attention to unimportant ones. Self-attention, alternatively termed intra-attention, permits input features to be evaluated by the attention mechanism itself. The self-attention score $S \in \mathbb{R}^{N \times 1}$ is computed using the following formula, N represents the number of edges:

$$S_{ij}^{h, l+1, (r_1, r_2]} = \text{linear} \left(\left\|_{k=1, 2, \dots, K} \sigma \left(\mathbf{z}_{ij}^{h, l, (r_1, r_2]} \mathbf{W}_f^k + b_f^k \right) \odot \mathbf{g} \left(\mathbf{z}_{ij}^{h, l, (r_1, r_2]} \mathbf{W}_s^k + b_s^k \right) \right\| \right) \quad (2)$$

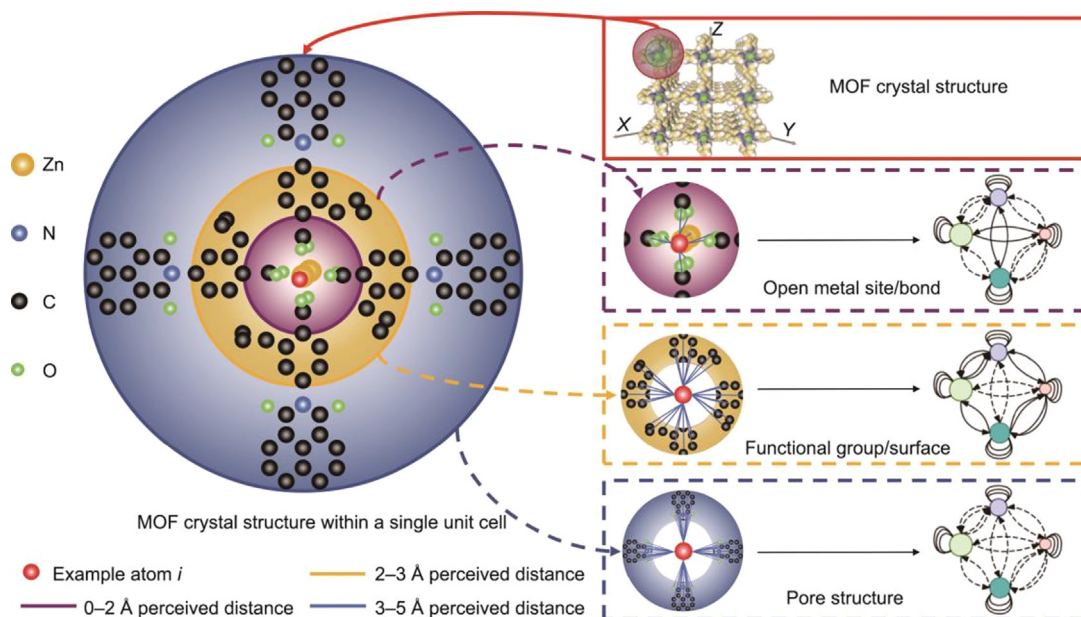


Fig. 2. Illustration of the multi-scale graph.

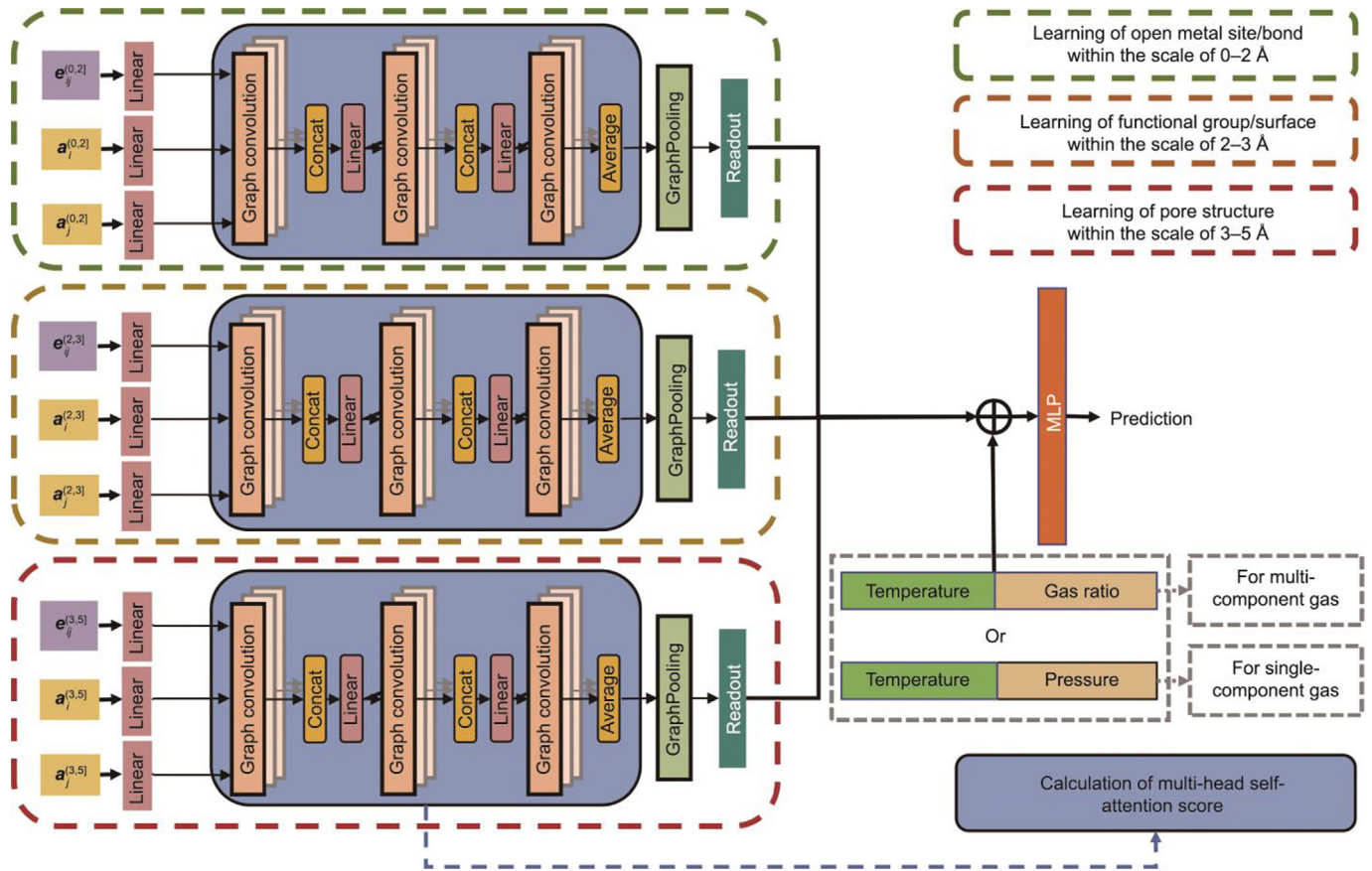


Fig. 3. Illustration of the detailed architecture for MHACGN-MS. Concat: concatenate; $e_{ij}^{(r_1, r_2)}$: the edge feature vector of the edge connecting nodes i and j in range $(r_1, r_2]$.

$$\mathbf{z}_{ij}^{h,l,(r_1, r_2]} = \begin{cases} \text{linear}(\mathbf{a}_i) \oplus \text{linear}(\mathbf{a}_j) \oplus S_{ij}^{h,l,(r_1, r_2]}, & l > 0 \\ \text{linear}(\mathbf{a}_i) \oplus \text{linear}(\mathbf{a}_j) \oplus \mathbf{e}_{ij}^{h,l,(r_1, r_2]}, & l = 0 \end{cases} \quad (3)$$

where $\sigma(\cdot)$ and $g(\cdot)$ are the activation functions sigmoid and softplus. K is the number of attention heads. W_f^k and W_s^k , b_f^k and b_s^k are the weights and bias parameters corresponding to the k th attention head used to perform linear transformation on the input before activation. Among them, the subscripts f and s respectively mean first and second, and they are only used as indices to distinguish between two parallel weights and biases. \odot represents multiplication by the element. $\parallel_{k=1,2,\dots,K}$ is a multiple concatenation operation that concatenates the calculation results of the attention heads from the 1st to the K th. $S_{ij}^{h,l+1,(r_1, r_2]}$ is the attention score of the h th edge connecting nodes i and j in range $(r_1, r_2]$ from the multi-head attention mechanism at layer $l+1$. \oplus represents concatenation operation. We concatenated \mathbf{a}_i , \mathbf{a}_j , and the $S_{ij}^{h,l,(r_1, r_2]}$ (if $l = 0$, then the $\mathbf{e}_{ij}^{h,l,(r_1, r_2]}$ instead) as vectors $\mathbf{z}_{ij}^{h,l,(r_1, r_2]}$ from the multi-head attention mechanism at layer l ; the attention score $S_{ij}^{h,l,(r_1, r_2]}$ was then obtained using Eq. (2).

$\sigma(\cdot)$ and $g(\cdot)$ are the activation functions used to introduce non-linear coupling between convolutional layers. We evaluated the impact of different activation function combinations on the gas adsorption prediction performance of the MHACGN-MS model for single-component (CO_2) and multi-component (CO_2 in CO_2/N_2 mixture) gases, as shown in Table S3 in Appendix A. As indicated in the table, the sigmoid + softplus configuration achieved excellent performance due to its collaborative nature in handling complex graphical structured data. The softplus activation function possesses smoothness and can maintain stability during the opti-

mization process. The output of the sigmoid function lies between 0 and 1 and has probabilistic interpretability, allowing $\sigma(\cdot)$ to serve as a learned weight matrix to distinguish interactions between adjacent nodes. In contrast, the tanh activation function suffers from a more severe problem of vanishing gradients. The rectified linear unit (ReLU) and LeakyReLU activation functions are simpler to compute but are more sensitive to weight initialization, which may even lead to issues such as vanishing or exploding gradients. After comprehensive consideration, we decided to choose the softplus activation function for $g(\cdot)$ and the sigmoid function for $\sigma(\cdot)$.

4.2. Edge selection (masking)

The GraphPooling layer adopts the edge selection method and retains part of the edges in the input graph:

$$\text{idx} = \text{Top_rank}(S, [k_p N]) \quad (4)$$

$$S_{\text{mask}} = S_{\text{idx}}, S_{\text{mask}} \in \mathbb{R}^{k_p N \times 1} \quad (5)$$

where the pooling ratio k_p is a super parameter, which determines the number of edges to be reserved; the top $[k_p N]$ edges are selected according to the value of the attention score S ; $\text{Top_rank}(\cdot)$ is a function that returns the index of the edges of the top $[k_p N]$; idx is the index set of top- $[k_p N]$ edges, obtained via the $\text{Top_rank}(S, [k_p N])$ operation, serving as an indexing tool to select these edges; and S_{mask} is a feature attention mask.

The impact of the pooling ratio k_p on the prediction performance deserves further discussion. Therefore, we evaluated k_p values of 0.3, 0.5, 0.6, 0.7, 0.8, 0.9, and 1.0, as outlined in Section S4 in Appendix A, to determine the optimal setting as 0.6. The pooling ratio k_p modulates the trade-off between feature retention and

computational efficiency. Optimal values (maximal coefficient of determination (R^2) and minimal root mean squared error (RMSE)) are bolded in Tables S4–S6 in Appendix A. As k_p increased from 0.3 to 1.0, the R^2 values across the training/validation/test sets peaked at $k_p = 0.6$, exhibited minor fluctuations at $k_p = 0.7–0.9$, and dropped sharply at $k_p = 1.0$. This pattern underscores the necessity of balancing information preservation with noise suppression. When k_p ranges between 0.6 and 0.9, the model demonstrated stable performance with synchronized R^2 trends in the training/validation sets, indicating negligible overfitting. At this range, k_p simplifies the graph topology by pruning weakly connected edges, thereby reducing noise while retaining critical nodes and strong interactions—providing a robust foundation for local feature learning. Conversely, performance deterioration at $k_p = 1.0$ likely results from noise accumulation, whereas suboptimal results at $k_p = 0.3$ stem from feature omission (e.g., critical interatomic interactions), which impairs subsequent layers' ability to capture crystalline structural patterns.

After obtaining the feature attention mask S_{mask} and the index of the edges with the top-ranking attention score $[k_p N]$, the GraphPooling layer performs a graph pooling operation.

$$\mathbf{E}_{\text{out}} = \mathbf{E}_{\text{idx}} \quad (6)$$

$$\text{EI}_{\text{out}} = \begin{bmatrix} \text{EI}[0][\text{idx}] \\ \text{EI}[1][\text{idx}] \end{bmatrix} \quad (7)$$

where $\mathbf{E} \in \mathbb{R}^{N \times d_e}$ is the edge feature matrix, $\mathbf{E}_{\text{idx}} \in \mathbb{R}^{k_p N \times d_e}$ is the edge feature matrix of top- $[k_p N]$ edges, $\mathbf{E}_{\text{out}} \in \mathbb{R}^{k_p N \times d_e}$ is the output edge feature matrix after indexing operation, $\text{EI} \in \mathbb{Z}^{2 \times N}$ is the edge index, $\text{EI}_{\text{out}} \in \mathbb{Z}^{2 \times k_p N}$ is the output edge index after indexing operation.

Because the self-attention score is obtained by using the feature information of the graph nodes and edges, the result of the pooling layer is based on the features and topology of the graph.

4.3. Node update

After processing three multi-scale images through the GraphPooling layers, we fuse them to construct a crystal graph, update the node features \mathbf{a}_i via graph convolution layers, generate the overall feature vector \mathbf{v}_c of the crystal, and concatenate it with external parameters such as temperature T , pressure P , and the adsorbed gas features \mathbf{v}_{gas} to obtain prediction results through the MLP layer.

$$\mathbf{e}_{ij}^* = \mathbf{e}_{ij}^{*(0,2)} \oplus \mathbf{e}_{ij}^{*(2,3)} \oplus \mathbf{e}_{ij}^{*(3,5)} \quad (8)$$

$$\mathbf{a}_i^* = \text{Conv}(\mathbf{a}_i, \mathbf{a}_j, \mathbf{e}_{ij}^*) \quad (9)$$

$$\mathbf{v}_c = \text{Average.Pool}(\mathbf{a}_0^*, \mathbf{a}_1^*, \dots, \mathbf{a}_M^*) \quad (10)$$

$$\text{Output} = \text{MLP}(\mathbf{v}_c \oplus T \oplus P) \quad (11)$$

Table 2
Performance of different graph neural networks on the test sets of single-component gases.

Algorithm	CH ₄		CO ₂		N ₂	
	RMSE	R^2	RMSE	R^2	RMSE	R^2
MHACGN-MS	0.7876	0.8353	1.1881	0.9203	0.4093	0.8438
GCN	1.0200	0.7343	2.0157	0.7533	0.5109	0.7843
GAT	1.4872	0.4288	3.2215	0.2981	0.6165	0.6816
GIN	0.9217	0.7885	1.2268	0.8944	0.4488	0.8275
CGCNN	0.8624	0.8222	1.4235	0.8524	0.4452	0.8304
MEGNet	0.8780	0.8087	≫100	≪−100	0.5021	0.7850
MPNN	0.9906	0.7372	1.4994	0.8443	0.7374	0.5118
MHACGN	0.8347	0.8244	1.4304	0.8786	0.4895	0.8128

where $\mathbf{e}_{ij}^{*(r_1, r_2)}$ represents the feature vectors of edges between nodes i and j in range $(r_1, r_2]$ after edge selection. \mathbf{e}_{ij}^* represents the final edge feature vectors obtained by concatenating all the preserved edge feature vectors $\mathbf{e}_{ij}^{*(r_1, r_2)}$ between nodes i and j . \mathbf{a}_i^* represents the update feature vector of node i obtained through graph convolutional layers.

5. Results and discussion

5.1. Model performance and validation

In this section, we apply other classical graphical convolutional network models, including GCN [27], GAT [28], GIN [26], CGCNN [29], MEGNet [30], MPNN [31], and MHACGN (the single-scale version of MHACGN-MS), together with MHACGN-MS, to predict the adsorption of MOFs for single-component gases (CH₄, CO₂, and N₂) at 6–30 bar and for multi-component gases (CH₄:N₂, CO₂:N₂, and CH₄:CO₂) under a gas ratio of 0.1:0.9 to 0.5:0.5. We then compare the predicted performance.

We randomly divided the MOF dataset into training, validation, and test sets at a ratio of 80:5:15. The training set served for the training and parameter optimization of the models, the validation set served for hyperparameter selection, and the test set served for evaluating the models' predictive accuracy for new data. We used RMSE and R^2 as evaluation indexes to calculate the accuracy of different models in predicting adsorption on the training, validation, and test sets.

5.1.1. Performance of models in predicting the adsorption of single-component gases

Table 2 shows the performance of different graph neural networks, including MHACGN-MS, on the test sets of CH₄, CO₂, and N₂. We compared the performance of seven graph neural networks in predicting single- and multi-component gas adsorption. The performance of predicting single-component gas adsorption on the training set and validation set is shown in Tables S7 and S8 in Appendix A. The performance of predicting multi-component gas adsorption on the training set and validation set is shown in Tables S9 and S10 in Appendix A.

Considering Table 2, as well as Tables S7 and S8, it is evident that MHACGN-MS performs the best on all the test sets of CH₄, CO₂, and N₂. In the remaining models, the neural networks specifically designed for crystal materials—namely, MHACGN, CGCNN, and MPNN—outperform GAT and GCN. Interestingly, GIN performs equally well, possibly due to its effective capture of both local and global graph structural information via injective properties, enhancing its processing of complex crystal material graphs. When predicting the adsorption performance of CO₂, MEGNet performed normally on the training set in Table S7 (RMSE=1.5538, $R^2=0.8374$) and the validation set in Table S8 (RMSE=1.7063, $R^2=0.8050$); however, when switching to the test set, both the RMSE and R^2 indicators were extremely poor (RMSE≫100,

$R^2 \ll -100$), indicating overfitting. This may be because the global environmental pooling layer of MEGNet cannot effectively capture global information in the presence of complex crystal structures and redundant atomic interactions but instead experiences noise interference. Based on the results from the training, validation, and test sets, MHACGN-MS demonstrated the best overall performance, effectively mitigating the issue of redundant atomic interference.

5.1.2. Performance of models in predicting the adsorption of multi-component gases

Table 3 shows the performance of different graph neural networks, including MHACGN-MS, on the test sets for multi-component gases ($\text{CH}_4:\text{CO}_2$, $\text{CO}_2:\text{N}_2$, and $\text{CH}_4:\text{N}_2$).

Table 3, as well as Tables S9 and S10 in Appendix A, reveals that MHACGN-MS exhibits superior predictive performance for multi-component gas adsorption, with the highest R^2 and lowest RMSE values. Among the other evaluated models, MHACGN, CGCNN, and GCN perform satisfactorily. However, MPNN demonstrates significantly reduced accuracy in predicting CH_4 adsorption within a multi-component gas, while GAT struggles with CO_2 adsorption predictions. Both MPNN and GAT have limitations in effectively capturing the relevant local and global graph structural information critical for accurate gas adsorption predictions. MEGNet displays pronounced overfitting when predicting CH_4 adsorption in the $\text{CH}_4:\text{CO}_2$ mixture and N_2 adsorption in the $\text{CO}_2:\text{N}_2$ mixture. Similarly, GIN experiences notable overfitting in predicting N_2 adsorption within the $\text{CH}_4:\text{N}_2$ mixture. Compared with single-component gas adsorption, multi-component gas adsorption involves more intricate atomic interactions and interference, which we hypothesize as a potential cause for overfitting.

In addition, through comparison, we found that, for the same model, the multi-scale prediction performance was still better than that of the single-scale method. This is because single-scale complex crystal diagrams often require more parameters to capture the complex relationships between nodes during model training, and they contain redundant or noisy information that can interfere with the model's extraction of useful features. Multi-scale crystal maps can provide independent feature representations for each subgraph, allowing for a more detailed characterization of the intrinsic structure of the data and improving prediction accuracy.

From Table 2, it can be observed that most algorithms exhibit better prediction performance for CO_2 adsorption than for CH_4 and N_2 adsorption across the training, validation, and test sets. In the single-component gas adsorption prediction task, the models' prediction accuracy for CO_2 adsorption is significantly higher than that for CH_4 and N_2 . This macroscopic phenomenon can be preliminarily explained by differences in physical and chemical properties at the molecular level: The quadrupole moment of a CO_2 molecule is $\mu = 1.34 \times 10^{-29}$ C·m, but the quadrupole moments are approximately infinite for CH_4 ($\mu = 0$) and for N_2 ($\mu = 0$). In

addition, the polarizability of a CO_2 molecule ($\alpha = 2.91 \times 10^{-24}$, cm^3) is significantly higher than those of CH_4 ($\alpha = 2.59 \times 10^{-24}$, cm^3) and N_2 ($\alpha = 1.74 \times 10^{-24}$, cm^3). The strong polarity characteristic of CO_2 leads to more significant induced dipole–dipole interactions (i.e., van der Waals forces) between CO_2 molecules and MOF frameworks, forming a distinct adsorption energy distribution pattern. When the algorithm captures this feature, it can prioritize establishing discrimination criteria for CO_2 during the training process. Therefore, within the same sampling range (298 K, 6–30 bar), the interatomic interactions related to CO_2 adsorption are more easily captured by a model, leading to more accurate predictions.

When a MOF adsorbs mixed gases, variations in molecular kinetic diameters (CH_4 : 0.380 nm; N_2 : 0.364 nm; CO_2 : 0.330 nm) and shape factors (tetrahedral CH_4 vs linear N_2/CO_2) generate distinct diffusion pathways within the MOF's pores. Specifically, CH_4 's larger molecular volume and tetrahedral geometry induce steric hindrance effects, while N_2 's smaller size and linear structure facilitate rapid micropore migration. These differential diffusion behaviors intensify the competition for adsorption sites among the gas species, making it more difficult to predict adsorption. Consequently, all algorithms show varying degrees of performance decline when predicting multi-component gas adsorption compared with single-component gas adsorption. It is evident that MHACGN-MS performs better in predicting CO_2/N_2 gas mixtures than in predicting CO_2/CH_4 and CH_4/N_2 mixtures. Moreover, in the adsorption predictions for the CO_2/CH_4 and CH_4/N_2 gas mixtures, MHACGN-MS demonstrates significantly stronger prediction performance for CO_2 and N_2 than for CH_4 . Additionally, GCN, GIN, CGCNN, MEGNet, and MPNN exhibit similar trends in predicting different multi-component gas adsorptions, albeit with less accuracy than MHACGN-MS. We interpret these findings as follows:

(1) Since MOFs generally have much a lower adsorption capacity for N_2 than for CO_2 , the competitive adsorption phenomenon in CO_2/N_2 mixtures is weaker, allowing CO_2 to dominate the adsorption process and thus simplifying the difficulty of adsorption prediction.

(2) Among the three gases, MOFs generally exhibit a stronger adsorption capacity for CO_2 and a weaker adsorption capacity for N_2 . This results in the competitive adsorption phenomenon in CO_2/CH_4 and CH_4/N_2 mixtures having a limited impact on the adsorption of CO_2 and N_2 , but interfering significantly with CH_4 . Consequently, predicting the adsorption of gas mixtures involving CH_4 becomes more complex and challenging.

For a more in-depth analysis of the model's reliability, we utilized the calculated adsorption data for N_2 on CoRE MOFs from the online nanoporous materials database provided by Bobbitt et al. [45] (77 K, 0–1 bar) to supplement our analysis of the model's performance under a wider range of conditions.

The dataset used in Tables 2 and 3 consists of adsorption data at five sampling points within the range of 6–30 bar for each MOF,

Table 3
Performance of different graph neural networks on the test sets of multi-component gases.

Algorithm	$\text{CH}_4:\text{CO}_2$				$\text{CO}_2:\text{N}_2$				$\text{CH}_4:\text{N}_2$			
	RMSE		R^2		RMSE		R^2		RMSE		R^2	
	CH_4	CO_2	CH_4	CO_2	CO_2	N_2	CO_2	N_2	CH_4	N_2	CH_4	N_2
MHACGN-MS	2.1179	0.6057	0.7120	0.8626	1.2152	0.6645	0.8778	0.8206	1.0037	0.3638	0.7073	0.8012
GCN	2.0544	0.8261	0.6717	0.7284	1.7275	0.7519	0.7625	0.7310	1.0304	0.4398	0.6791	0.7198
GAT	2.2864	1.3838	0.5677	0.2349	3.4917	0.9393	0.0397	0.6221	1.4177	0.5050	0.4147	0.6000
GIN	2.1154	0.6738	0.6860	0.8222	1.5064	0.6840	0.8402	0.8086	>100	0.3718	<<-100	0.7852
CGCNN	2.0887	0.6776	0.6744	0.8163	1.6545	0.7112	0.7771	0.7837	1.0265	0.3691	0.7029	0.7962
MEGNet	10.6974	0.7052	-7.3358	0.8025	1.6702	>100	0.7612	<<-100	1.3333	0.4033	0.5129	0.7470
MPNN	3.0218	0.8802	0.3758	0.6975	1.4561	1.0298	0.8237	0.5159	1.6083	0.4186	0.1977	0.7364
MHACGN	2.2157	0.6404	0.6997	0.8361	1.5273	0.7078	0.8024	0.7769	1.0571	0.3753	0.6819	0.7980

while the dataset in Table 4 comprises adsorption data at six sampling points within the range of 0–1 bar for each MOF. Almost all models showed improved performance in Table 4 compared with Table 2. We speculate that this may be due to the denser distribution of sampling points in the dataset used in Table 4, which is more conducive to the model learning the structure–property relationships of MOFs. It is worth noting that, under different pressure and temperature conditions, MHACGN-MS consistently outperformed the other models, validating the robustness of the MHACGN-MS model.

5.2. Interpretability of the model

The MHACG-MS model emphasizes atomic interactions across the scales of 0–2, 2–3, and 3–5 Å, assigning attention scores and performing pooling accordingly. To illustrate model interpretability in adsorption performance, we visualized atomic interactions at different scales based on attention scores. Fig. 4 showcases two representative MOFs with high CO₂ adsorption capacities (>8 mol·kg⁻¹). Atomic interactions within 0–2, 2–3, and 3–5 Å are depicted by red, green, and purple edges, respectively. Edge color intensity reflects the attention score assigned by the model, with darker colors indicating higher scores and lighter colors indicating lower scores. Unit cells of different crystals vary in size. For the convenience of comparison and display, Fig. 4 adopts a fractional coordinate system. The fractional coordinates are based on

Table 4
Performance of different graph neural networks on the sets for N₂ at 77 K, 0–1 bar.

Algorithm	Training set		Validation set		Test set	
	RMSE	R ²	RMSE	R ²	RMSE	R ²
MHACGN-MS	0.8494	0.9814	0.4664	0.9925	0.8705	0.9806
GCN	1.5376	0.9371	1.8538	0.9257	2.0145	0.8947
GAT	3.7459	0.6389	5.2616	0.4300	3.8313	0.5456
GIN	1.9176	0.9051	0.9745	0.9300	1.7439	0.9308
CGCNN	1.2437	0.9581	1.5088	0.9435	1.3890	0.9575
MEGNet	2.1384	0.8850	1.3707	0.8880	2.0831	0.8828
MPNN	1.8696	0.9091	1.8369	0.9070	1.9414	0.9025
MHACGN	1.3681	0.9498	1.4068	0.9679	1.3381	0.9503

the edge lengths and axis system of the unit cell, with the lengths of the three basis direction vectors ℓ_1 , ℓ_2 , and ℓ_3 of the unit cell taken as the unit lengths for each axis, respectively. The coordinate range is 0 to 1, with no physical units, representing the relative positions of atoms within the unit cell.

Taking the two MOFs PEVPUD and XAWVUN as examples, we plotted heat maps of attention weights for interatomic interactions at different scales to explore the underlying mechanisms of gas adsorption. It is worth mentioning that, due to the large number of atoms in MOFs, we only depicted interactions with normalized attention weights greater than 0.1 in the heat maps to ensure readability.

From Fig. 5(a), combined with the 3D visualization of attention weights in Fig. 4 and the corresponding atom types based on their identifiers (IDs), which match the stored order of the atoms in the node list of the crystal graph in the MOF, it can be observed that, when the attention scale is 0–2 Å, the pairs with higher attention weights are Zn–O and C–O; at the scale of 2–3 Å, Zn–C pairs and some C–C pairs located on aromatic rings exhibit higher attention weights; and at the scale of 3–5 Å, Zn–C and Zn–O pairs have higher attention weights.

In other words, for PEVPUD, when the attention scale is 0–2 Å, the model primarily focuses on metal–oxygen bridges and C=O bonds that can serve as CO₂ adsorption sites; at the scale of 2–3 Å, the model starts to pay attention to metal–carbon coordination bonds closely related to MOF structural stability and pore surfaces, as well as aromatic functional groups capable of forming π – π interactions or van der Waals forces with gas molecules; and at the scale of 3–5 Å, the model focuses on the interactions between metal atoms and carbon/oxygen atoms in organic ligands that constitute the basic framework of the MOF, thereby learning the overall pore structure of the MOF.

For XAWVUN, when the attention scale is 0–2 Å, the model primarily focuses on Cu–C pairs serving as adsorption sites and some C–C pairs located on aromatic rings; when the attention scale is 2–3 Å, the model pays more attention to Cu–C pairs related to structural stability and pore surfaces; and when the attention scale is 3–5 Å, the model mainly focuses on Cu–O, C–H, and H–H pairs. Unlike PEVPUD, the model only learns the metal–oxygen bridges of XAWVUN as adsorption sites in the scale range of 3–5 Å; this is because

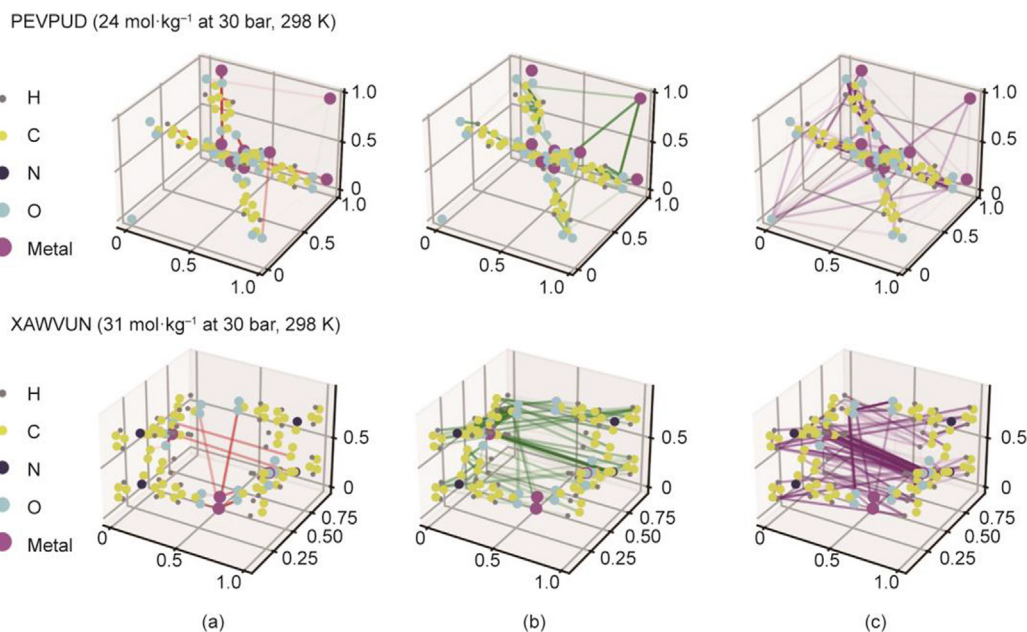


Fig. 4. Visualization of attention scores for interatomic interactions at different scales: (a) 0–2 Å; (b) 2–3 Å; and (c) 3–5 Å.

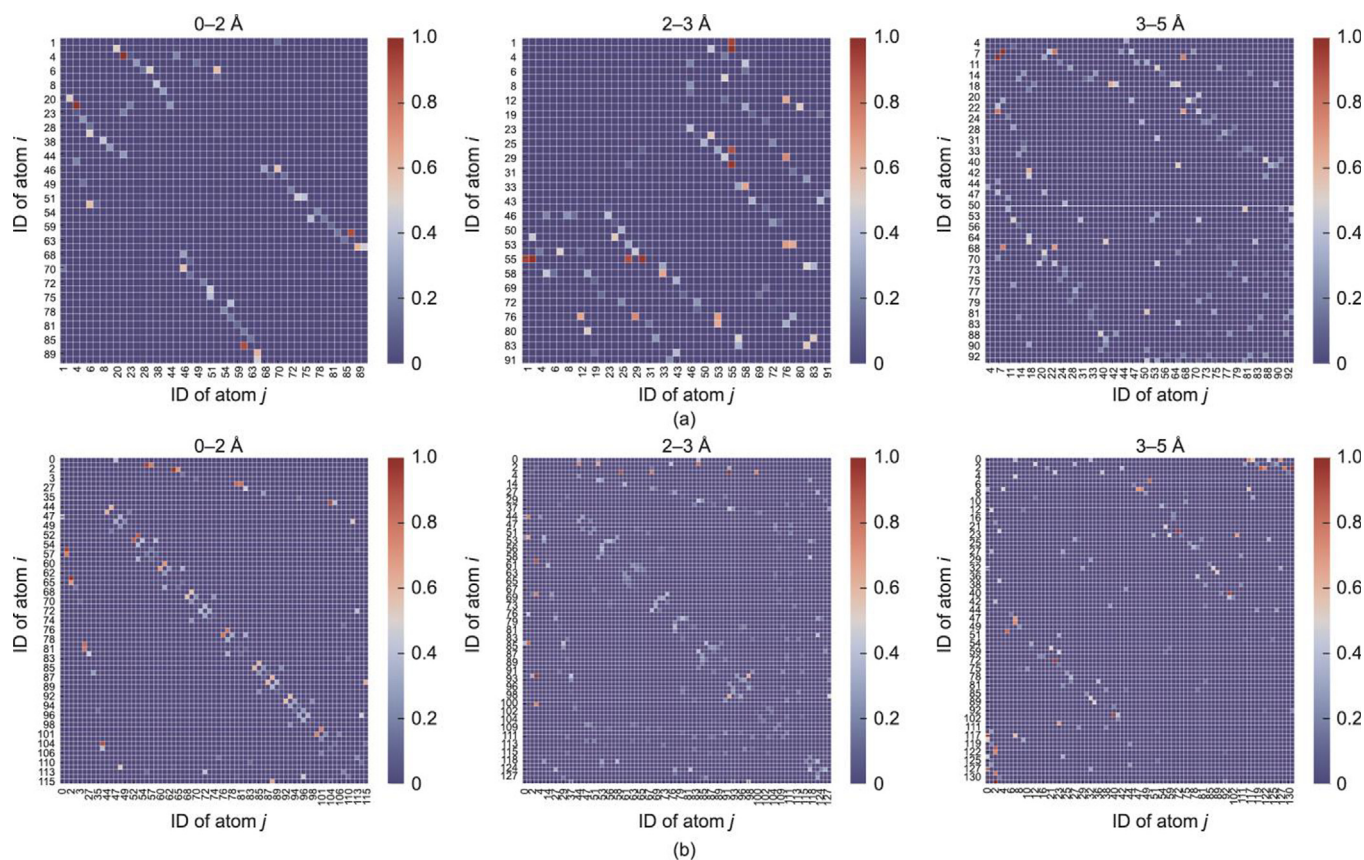


Fig. 5. Heat maps of attention weights for interatomic interactions at different scales. Using the atomic IDs in the MOF as the coordinate axes, the color blocks represent the attention weight scores of the interatomic forces between different atoms. The higher the weight score, the redder the block; the lower the weight score, the bluer the block. (a) Heat maps of PEVPUD with the correspondence between atomic IDs and atomic types (Zn: 0–7; H: 8–19; C: 20–67; O: 68–93). (b) Heat maps of XAWVUN with the correspondence between atomic IDs and atomic types (Cu: 0–3; H: 4–43; C: 44–111; N: 112–115; O: 116–131).

the bond lengths of metal–oxygen bridges can vary depending on factors such as metal type, oxidation state, coordination environment, and specific compound structure. Additionally, parallel aromatic rings at an appropriate distance (>3.5 Å) can increase the adsorption force on gas molecules through π – π interactions [46]. In conjunction with Fig. 4, we are delighted to observe that the model indeed explores this feature by learning the interactions between atom pairs (C–H and H–H pairs) with atoms located on parallel aromatic rings at both ends.

6. Conclusions

In this paper, we proposed a multi-scale crystal graph for describing periodic crystal structure and a multi-scale graph neural network named MHACGN-MS that combines multi-head self-attention graph pooling layers for multi-scale crystal graphs. The proposed model learns the structural characteristics of periodic crystal structures at different scales by allocating attention to interatomic interactions at different scales, thereby reducing interference from redundant interatomic interactions. By comparing it with other traditional graph neural network methods, we demonstrated that MHACGN-MS achieved the highest accuracy in predicting single- and multi-component gas adsorption. In addition, we demonstrated the interpretability of MHACGN-MS. We showed its effective learning of MOF structural features at different scales through the layer-by-layer visualization of graph neural networks. MHACGN-MS provides a novel, efficient, multi-level, and interpretable perspective for the attribute prediction of complex porous crystal structures such as MOFs using deep learning algorithms.

Furthermore, based on the comparison and analysis of adsorption predictions for different types of gas molecules in this article, we propose exploration directions for future algorithm application. For CO_2 -centric separations (e.g., carbon capture), architectures emphasizing quadrupole feature learning should be prioritized. For CH_4 purification, molecular-volume-sensitive extractors are warranted. For future research, we can also construct a multi-physics coupled dataset that explicitly encodes multidimensional features such as molecular polarity, size, and shape. This refined research paradigm not only helps to break through the performance bottleneck of current algorithms but also provides theoretical support for the high-throughput screening of MOF materials.

CRedit authorship contribution statement

Lujun Li: Software, Investigation, Validation, Methodology, Conceptualization, Writing – original draft. **Haibin Yu:** Writing – review & editing, Resources, Project administration, Supervision, Conceptualization, Funding acquisition.

Declaration of competing interest

The authors declare that they have no known competing financial interests or personal relationships that could have appeared to influence the work reported in this paper.

Acknowledgment

This work was supported by the National Natural Science Foundation of China (NSFC) (61821005).

Appendix A. Supplementary data

Supplementary data to this article can be found online at <https://doi.org/10.1016/j.eng.2025.08.012>.

References

- Alezi D, Belmabkhout Y, Suyetin M, Bhatt PM, Weseliński LJ, Solovyeva V, et al. MOF crystal chemistry paving the way to gas storage needs: aluminum-based soc-MOF for CH₄, O₂, and CO₂ storage. *J Am Chem Soc* 2015;137(41):13308–18.
- Listyarini RV, Gamper J, Hofer TS. Storage and diffusion of carbon dioxide in the metal organic framework MOF 5—a semi-empirical molecular dynamics study. *J Phys Chem B* 2023;127(43):9378–89.
- Zhang L, Song L, Meng LL, Guo YN, Zhu XY, Qin LZ, et al. Anionic Ni-based metal–organic framework with Li(I) cations in the pores for efficient C₂H₂/CO₂ separation. *ACS Appl Mater Interfaces* 2024;16(1):847–52.
- Fu XP, Le XY, Xiao YH, Zeng DM, Zhou KA, Huang L, et al. Cucurbituril-shaped Cd₁₈(triazolate)₁₂ unit-based metal–organic framework exhibiting an C₂H₂/CO₂ separation ability. *Inorg Chem* 2023;62(37):15031–8.
- Eskemech A, Chand H, Karmakar A, Krishnan V, Koner RR. Zn-MOF as a single catalyst with dual Lewis acidic and basic reaction sites for CO₂ fixation. *Inorg Chem* 2024;63(8):3757–68.
- Wang Q, Wang H, Ren X, Pang R, Zhao X, Zhang L, et al. Synergetic role of thermal catalysis and photocatalysis in CO₂ reduction on Cu₂/MoS₂. *J Phys Chem Lett* 2023;14(38):8421–7.
- Muddassar M, Alarifi A, Abduh NAY, Saeed WS, Karami AM, Afzal M. Multifunctional Zn(II) coordination polymer as highly selective fluorescent sensor and adsorbent for dyes. *Int J Mol Sci* 2023;24(10):8512.
- Casanova-Chafer J, Garcia-Aboal R, Llobet E, Atienzar P. Enhanced CO₂ sensing by oxygen plasma-treated perovskite–graphene nanocomposites. *ACS Sens* 2024;9(2):830–9.
- Zhang H, Snurr RQ. Computational study of water adsorption in the hydrophobic metal–organic framework ZIF-8: adsorption mechanism and acceleration of the simulations. *J Phys Chem C* 2017;121(43):24000–10.
- Chen C, Zhang M, Zhang W, Bai J. Stable amide-functionalized metal–organic framework with highly selective CO₂ adsorption. *Inorg Chem* 2019;58(4):2729–35.
- Gülsoy Z, Sezginel KB, Uzun A, Keskin S, Yıldırım R. Analysis of CH₄ uptake over metal–organic frameworks using data-mining tools. *ACS Comb Sci* 2019;21(4):257–68.
- Fernandez M, Woo TK, Wilmer CE, Snurr RQ. Large-scale quantitative structure–property relationship (QSPR) analysis of methane storage in metal–organic frameworks. *J Phys Chem C* 2013;117(15):7681–9.
- Qiao Z, Yan Y, Tang Y, Liang H, Jiang J. Metal–organic frameworks for xylene separation: from computational screening to machine learning. *J Phys Chem C* 2021;125(14):7839–48.
- Shi K, Li Z, Anstine DM, Tang D, Colina CM, Sholl DS, et al. Two-dimensional energy histograms as features for machine learning to predict adsorption in diverse nanoporous materials. *J Chem Theory Comput* 2023;19(14):4568–83.
- Deringer VL, Bartók AP, Bernstein N, Wilkins DM, Ceriotti M, Csányi G. Gaussian process regression for materials and molecules. *Chem Rev* 2021;121(16):10073–141.
- Osaro E, Mukherjee K, Colón YJ. Active learning for adsorption simulations: evaluation, criteria analysis, and recommendations for metal–organic frameworks. *Ind Eng Chem Res* 2023;62(33):13009–24.
- Zhang L, Huang Q, Li L, Yan Y, Yuan X, Liang H, et al. Automatic machine learning combined with high-throughput computational screening of hydrophobic metal–organic frameworks for capture of methanol and ethanol from the air. *ACS ES T Eng* 2024;4(1):115–27.
- Fernandez M, Barnard AS. Geometrical properties can predict CO₂ and N₂ adsorption performance of metal–organic frameworks (MOFs) at low pressure. *ACS Comb Sci* 2016;18(5):243–52.
- Anderson R, Biang A, Gómez-Gualdrón DA. Adsorption predictions for multiple molecules in MOFs using the same deep learning model. *J Chem Theory Comput* 2020;16(2):1271–83.
- Goeminne R, Vanduyfhuys L, Van Speybroeck V, Verstraelen T. DFT-quality adsorption simulations in metal–organic frameworks enabled by machine learning potentials. *J Chem Theory Comput* 2023;19(18):6313–25.
- Zhang Z. Automated graph neural networks accelerate the screening of optoelectronic properties of metal–organic frameworks. *J Phys Chem Lett* 2023;14(5):1239–45.
- Chen H, Zheng Y, Li J, Li L, Wang X. AI for nanomaterials development in clean energy and carbon capture, utilization and storage (CCUS). *ACS Nano* 2023;17(11):9763–92.
- Ma R, Colón YJ, Luo T. Transfer learning study of gas adsorption in metal–organic frameworks. *ACS Appl Mater Interfaces* 2020;12(30):34041–8.
- Park H, Kang Y, Kim J. Enhancing structure–property relationships in porous materials through transfer learning and cross-material few-shot learning. *ACS Appl Mater Interfaces* 2023;15(48):56375–85.
- Peng J, Schwalbe-Koda D, Akkiraju K, Xie T, Giordano L, Yu Y, et al. Human- and machine-centred designs of molecules and materials for sustainability and decarbonization. *Nat Rev Mater* 2022;7(12):991–1009.
- Xu K, Hu W, Leskovec J. How powerful are graph neural networks? In: Proceedings of the 7th International Conference on Learning Representations; 2019 May 6–9; New Orleans, LA, USA. Red Hook: Curran Associates, Inc.; 2019. p. 1–17.
- Kipf TN, Welling M. Semi-supervised classification with graph convolutional networks. In: Proceedings of the 5th International Conference on Learning Representations; 2017 Apr 24–26; Toulon, France. Red Hook: Curran Associates, Inc.; 2017. p. 2713–27.
- Veličković P, Cucurull G, Casanova A, Romero A, Liò P, Bengio Y. Graph attention networks. In: Proceedings of the 6th International Conference on Learning Representations; 2018 Apr 30–May 3; Vancouver, BC, Canada. Red Hook: Curran Associates, Inc.; 2018. p. 1–12.
- Xie T, Grossman JC. Crystal graph convolutional neural networks for an accurate and interpretable prediction of material properties. *Phys Rev Lett* 2018;120(14):145301–7.
- Chen C, Ye W, Zuo Y, Zheng C, Ong SP. Graph networks as a universal machine learning framework for molecules and crystals. *Chem Mater* 2019;31(9):3564–72.
- Gilmer J, Schoenholz SS, Riley PF, Vinyals O, Dahl GE. Neural message passing for quantum chemistry. *PMLR* 2017;70:1263–72.
- Yan K, Liu Y, Lin Y, Ji S. Periodic graph transformers for crystal material property prediction. In: Koyejo S, Mohamed S, Agarwal A, Belgrave D, Cho K, Oh A, editors. Advances in neural information processing systems 35: 36th Conference on Neural Information Processing Systems; 2022 Nov 28–Dec 9; New Orleans, LA, USA. Red Hook: Curran Associates, Inc.; 2022. p. 15066–80.
- Chen P, Jiao R, Liu J, Liu Y, Lu Y. Interpretable graph transformer network for predicting adsorption isotherms of metal–organic frameworks. *J Chem Inf Model* 2022;62(22):5446–56.
- Liu X, Wang R, Wang X, Xu D. High-throughput computational screening and machine learning model for accelerated metal–organic frameworks discovery in toluene vapor adsorption. *J Phys Chem C* 2023;127(23):11268–82.
- Chung YG, Haldoupis E, Bucior BJ, Haracz M, Lee S, Zhang H, et al. Advances, updates, and analytics for the computation-ready, experimental metal–organic framework database: CoRE MOF 2019. *J Chem Eng Data* 2019;64(12):5985–98.
- Thornton AW, Simon CM, Kim J, Kwon O, Deeg KS, Konstas K, et al. Materials genome in action: identifying the performance limits of physical hydrogen storage. *Chem Mater* 2017;29(7):2844–54.
- Willems TF, Rycroft CH, Kazi M, Meza JC, Haracz M. Algorithms and tools for high-throughput geometry-based analysis of crystalline porous materials. *Microporous Mesoporous Mater* 2012;149(1):134–41.
- Do D, Do H. Pore characterization of carbonaceous materials by DFT and GCMC simulations: a review. *Adsorpt Sci Technol* 2003;21(5):389–423.
- Dubbeldam D, Calero S, Ellis DE, Snurr RQ. RASPA: molecular simulation software for adsorption and diffusion in flexible nanoporous materials. *Mol Simul* 2016;42(2):81–101.
- Rappe AK, Casewit CJ, Colwell KS, Goddard III WAI, Skiff WM. UFF, a full periodic table force field for molecular mechanics and molecular dynamics simulations. *J Am Chem Soc* 1992;114(25):10024–35.
- Sumer Z, Keskin S. Ranking of MOF adsorbents for CO₂ separations: a molecular simulation study. *Ind Eng Chem Res* 2016;55(39):10404–19.
- Sezginel KB, Uzun A, Keskin S. Multivariable linear models of structural parameters to predict methane uptake in metal–organic frameworks. *Chem Eng Sci* 2015;124(14):125–34.
- Basdogan Y, Keskin S. Simulation and modelling of MOFs for hydrogen storage. *CrstEngComm* 2015;17(2):261–75.
- Potoff JJ, Siepmann JI. Vapor–liquid equilibria of mixtures containing alkanes, carbon dioxide, and nitrogen. *AIChE J* 2001;47(7):1676–82.
- Bobbitt NS, Shi K, Bucior BJ, Chen H, Tracy-Amoroso N, Li Z, et al. MOFX-DB: an online database of computational adsorption data for nanoporous materials. *J Chem Eng Data* 2023;68(2):483–98.
- Boyd PG, Chidambaram A, García-Díez E, Ireland CP, Daff TD, Bounds R, et al. Data-driven design of metal–organic frameworks for wet flue gas CO₂ capture. *Nature* 2019;576(7786):253–6.